Research Square

Preprints are preliminary reports that have not undergone peer review.
They should not be considered conclusive, used to inform clinical practice,
or referenced by the media as validated information.

Efficient Degradation of Rhodamine B by g-C3N4/CaCO3/BiOCl Composite Photocatalyst Adsorption under Visible-Light Irradiation

Xiaotong Zhang
Jilin Jianzhu University
Yutong Liu
Jilin Jianzhu University
Mingrui Fan
Jilin Jianzhu University
Ziyang Wan
Jilin Jianzhu University
Dawei Jiang
Jilin Jianzhu University
Huisheng Liu
Jilin Jianzhu University
Hengye Shi
Jilin Jianzhu University
Yujie Jin
jinyujie@jlju.edu.cn

Jilin Jianzhu University

Research Article

Keywords: CaCO3, BiOCl, g-C3N4, modification, Photocatalysis

Posted Date: November 20th, 2026

DOI: https://doi.org/10.21203/rs.3.rs-11616664/v1

License: This work is licensed under a Creative Commons Attribution 4.0 International License.
Read Full License

Additional Declarations: No competing interests reported.

Efficient Degradation of Rhodamine B by g-C_3N_4/$CaCO_3$/BiOCl Composite Photocatalyst Adsorption under Visible-Light Irradiation

Xiaotong Zhang, Yutong Liu, Mingrui Fan, Ziyang Wan, Dawei Jiang, Huisheng Liu, Hengye Shi, Yujie Jin*

School of Materials Science and Engineering, Jilin Jianzhu University, Changchun, Jilin 130118, China

*Corresponding author.

E-mail address:jinyujie@jlju.edu.cn(Yujie Jin)

Abstract: In this study, $CaCO_3$/BiOCl was first synthesized via a solvothermal method, and subsequently combined with g-C_3N_4 under magnetic stirring to fabricate g-C_3N_4/$CaCO_3$/BiOCl composite materials. The phase structure, morphology, functional groups, and optical absorption properties of the samples were characterized by XRD, SEM, FT-IR, and UV-Vis DRS, respectively. Under irradiation from a 300 W Xe lamp, with RhB as the model pollutant. The photocatalytic degradation efficiency of RhB over the g-C_3N_4/$CaCO_3$/BiOCl composite reached 98.81% within 60min, which is approximately 2.49 times and 1.38 times that of pure BiOCl and $CaCO_3$/BiOCl, respectively. After five consecutive cycling tests, the degradation efficiency still remained above 95%, demonstrating excellent photocatalytic stability. UV-Vis diffuse reflectance spectra (DRS) and Tauc Polt revealed that the composite photocatalyst possesses a narrow bandgap of 2.5 eV, indicative of enhanced visible-light absorption. Meanwhile, PL, TPC, and EIS confirmed the efficient separation of photogenerated electron-hole pairs. The combined effects of broadened light absorption and suppressed charge recombination, contributed to the significantly enhanced photocatalytic performance. Results suggest that the g-C_3N_4/$CaCO_3$/BiOCl composite material exhibits promising potential for application in photocatalytic degradation of wastewater pollutants.

Keywords：$CaCO_3$,BiOCl,g-C_3N_4,modification,Photocatalysis

Statements and Declarations:

Competing interests:The authors declare that they have no known competing financial interests or personal relationships that could have appeared to influence the work reported in this paper.

Funding:This work got financial support from the Science and Technology Research Project of the Education Department of Jilin Province (JJKH20250986KJ).

1. Introduction

With the development of the textile industry, water pollution has become increasingly severe, and human health problems have also increased. There are some weaknesses in traditional water treatment methods, such as high costs, inability to achieve expected degradation effects, and even the generation of other pollutants [1,2]. Compared with photocatalytic degradation, photocatalytic degradation is a more environmentally friendly measure that can undergo degradation reactions under sunlight conditions. It has the advantages of high efficiency, non-toxic and pollution-free, and has received widespread attention from researchers [3-9]. Among numerous photocatalytic materials, BiOX (X=F, Cl, Br, I) [10,11,12] photocatalysts have an open layered structure that provides sufficient polarization space for relevant atoms and orbitals, and generates an internal electrostatic field perpendicular to the $[Bi_2O_2]^{2+}$ layer and $[X]^-$ layer, which facilitates the separation of photo generated electrons and holes, thus attracting much attention [13,14]. Among all BiOX semiconductor materials, due to the wide bandgap of BiOCl (about 3.28eV), its response wavelength is located in the ultraviolet region, resulting in low photocatalytic efficiency. Researchers have explored various methods to improve the photocatalytic activity of this defect, including morphology control, ion doping, defect introduction, and heterojunction construction [15,16]. Yao et al. [17] reported the fabrication of three-dimensional BiOCl nanophotocatalysts modified with Au. Anirban et al.[18] prepared bismuth-doped bismuth oxyhalide solid-solution films via calcination. Metal doping narrows the band gap of bismuth oxyhalides and strengthens visible-light absorption, thereby improving the utilization efficiency of visible light. Yuan et al. [19] prepared ultra-thin nanosheets while introducing oxygen vacancies on the surface to expand the visible light absorption range and enhance the electron hole redox ability. Liu et al. [20] synthesized BiOCl/Bi_2S_3 composite materials, which showed a 25 fold increase in degradation activity compared to pure BiOCl. Combination of BiOX (X = F, Cl, Br, and I) and rGO that forms an ultrathin layered structure BiOX/rGO as a sulfur host [21]. However, most studies focus on single ion doping or composites, and there is a lack of research on the stability of material structures. It has been proven that the photocatalytic activity can be significantly improved by compounding with mineral materials [22,23].Tian et al. [22] used calcination method to composite BiOBr with kaolinite, increasing the surface oxygen content and improving the degradation efficiency of organic dyes. Liu et al. [23] synthesized BiOBr with palygorskite using hydrothermal method, which exhibited high photocatalytic oxidation ability under visible light, effectively separating photogenerated carriers and enhancing their photocatalytic activity. Zhang et al. [24] synthesized a heterojunction by combining zeolite with BiOCl, and the addition of zeolite increased the specific surface area of the photocatalyst, exhibiting excellent degradation effects on both Rh B and formaldehyde.

However, in most studies, issues such as the stability, sustainability, and preparation cost of materials in long-term use are generally overlooked. Calcite like $CaCO_3$ has stability and low cost, is environmentally friendly, and is often used as a catalyst carrier to improve the dispersion of the catalyst, increase its active sites, and enhance its photocatalytic ability [25,26]. Wang et al.[27] used $CaCO_3$ as a support for uniform dispersion of TiO_2. The composite photocatalyst displayed enhanced methyl-orange photodegradation performance and cycling stability. Hu et al.[28] prepared $CaCO_3$/BiOBr. Characterizations showed that $CaCO_3$ addition raised the specific surface area and photocatalytic activity, with 97% RhB degradation efficiency. Simply increasing the specific surface area cannot achieve excellent photocatalytic effects. g-C_3N_4 is a layered semiconductor photocatalytic material with a bandgap of approximately 2.7 eV, possessing thermal stability and corrosion resistance, which can be used to improve the wide bandgap of BiOCl [29,30]. Xu et al. [31] $BiFeO_3$/g-C_3N_4

composites were prepared. The photogenerated electrons of g-C_3N_4 transfer to $BiFeO_3$, which obviously improves the degradation efficiency of tetracycline..Yang et al. [32] Rationally designed S-scheme heterojunction of BiOCl/g-C_3N_4 and the photocatalytic degradation activity was much higher than that of pure g-C_3N_4 and BiOCl. The above experiments confirm that $CaCO_3$ can increase the specific surface area of the catalyst, and g-C_3N_4 can improve the problem of unfavorable absorption of visible light and recombination rate of photo generated carriers caused by the bandgap width of photocatalysts.Taking advantage of the advantages of various materials to form a new type of photocatalytic material with low cost, good stability, and high degradation rate is the topic we want to study.

This experiment uses the hot solvent method to prepare $CaCO_3$/BiOCl, and then adds a certain amount of g-C_3N_4 to prepare the g-C_3N_4/$CaCO_3$/BiOCl ternary composite photocatalyst by physical stirring method. The degradation mechanism is analyzed and the photocatalytic effect is explored. And RhB can mimic dye wastewater for water pollution degradation experiments. The results showed that the prepared composite photocatalyst improved photocatalytic activity and stability, providing a new method for wastewater treatment.

2. Methods

2.1 Reagents and materials

Bismuth nitrate pentahydrate($Bi(NO_3)_3·5H_2O$), potassium chloride(KCl), anhydrous calcium chloride ($CaCl_2$), anhydrous calcium carbonate($CaCO_3$), melamine($C_3H_6N_6$), ethylene glycol($C_2H_6O_2$), anhydrous ethanol(C_2H_6O), RhB,BQ,IPA,$(NH_4)_2C_2O_4$ and $AgNO_3$ were all procured from Shanghai Aladdin Biochemical Technology Co., Ltd.

2.2 Preparation of samples

Synthesis of g-C_3N_4:

5g of melamine powder was placed in an alumina crucible, covered with a lid but not sealed, and then heated in a muffle furnace under static air. The temperature was ramped up to 550 °C at a rate of 5 °C/min and maintained for 4h. After the reaction, the furnace was allowed to cool naturally to room temperature. The resulting yellow powder was collected and ground, and denoted as CN.

Synthesis of $CaCO_3$/BiOCl composite:

0.334g of $CaCO_3$ was dispersed in 30 mL of absolute ethanol and stirred for 30 min. Then, 1.455g of $Bi(NO_3)_3·5H_2O$ was added into the suspension and stirring continued for another 30 min. Subsequently, 0.225g of KCl was introduced and the mixture was stirred for an additional 30min. The resulting mixture was transferred into a 100 mL Teflon-lined stainless steel autoclave and solvothermally treated at 160 °C for 12h. After natural cooling to room temperature, the precipitate was collected by filtration, washed several times with deionized water and absolute ethanol, and dried under vacuum at 60 °C for 12h. The final product was ground into powder and denoted as $CaCO_3$/BiOCl, and denoted as C/BC.

Synthesis of g-C_3N_4/$CaCO_3$/BiOCl:

Different amounts of g-C_3N_4 powder (0.0053g, 00111g, 0.0176g, 0.025g, 0.0333g) with various mass fractions and 0.1g of $CaCO_3$/BiOCl powders were dispersed in 40 mL deionized water and ultrasonicated for 30min. The $CaCO_3$/BiOCl suspension was slowly added dropwise into the g-C_3N_4 suspension, followed by another 30min of sonication. Afterwards, the mixed suspension was

magnetically stirred for another 30min. The mixture was aged statically, then the precipitate was washed, dried and ground to yield g-C_3N_4/$CaCO_3$/BiOCl powder samples, which were denoted as 5-CN/C/BC,10-CN/C/BC,15-CN/C/BC,20-CN/C/BC,25-CN/C/ BC.

2.3 Photocatalytic degradation experiments

The photocatalytic degradation activity of the samples was assessed using RhB as the model organic pollutant. A 300 W xenon lamp fitted with a 400 nm cut-off filter served as the visible light source. UV–vis spectrophotometry was utilized to monitor RhB concentrations and record the absorption spectra of the solutions.

3. Results and discussion

3.1 Photocatalyst characterisation

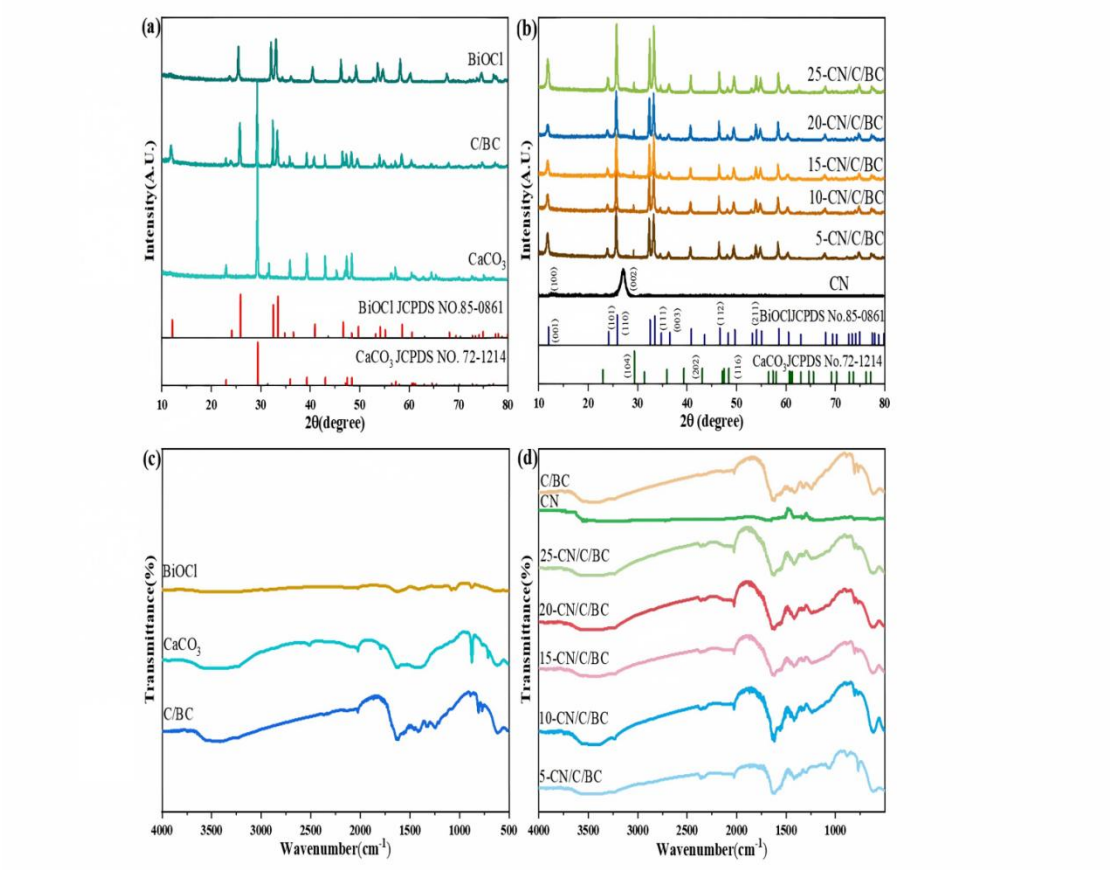


Fig. 1 (a) XRD patterns of BiOCl, $CaCO_3$, and C/BC composites; (b) patterns of X-CN/C/BC composites; (c) FT-IR spectra of BiOCl, $CaCO_3$, and C/BC composite materials; (d) FT-IR spectra of C/BC, CN, and X-CN/C/BC composite materials

X-ray diffraction (XRD) was employed to characterize the phase structure of the samples, and the obtained patterns were analyzed in detail. Fig. 1(a) displays the XRD patterns of pure BiOCl, pure $CaCO_3$ and C/BC composites. The diffraction peaks of C/BC appear at 2θ = 11.99°, 25.87°, 32.52°, 36.54°, and 40.91°, which correspond to the (001), (101), (110), (003), and (112) crystal planes of

tetragonal strained BiOCl(JCP DSNo.85-0861) [33]. The diffraction peak located at 2θ = 29.37°, 43.11°, 48.45°. The matches the (104), (202), and(116) characteristic peak of calcite-phase $CaCO_3$(JCPDSNO.72-1214) [34], which confirms the successful synthesis of C/BC composite. Fig. 1(b) presents the XRD patterns of CN/C/BC composites and pure CN with varying mass ratios of CN. Two sharp characteristic diffraction peaks of pure CN are observed at 2θ = 13.12° (100), and 2θ = 27.41° (002). The ternary CN/C/BC composite initially displays no prominent diffraction peaks assigned to CN. However, as the mass loading of CN rises, the peak intensity of CN/C/BC at 2θ = 25.87° (101) increases remarkably. This phenomenon can be attributed to enhanced nitrogen doping, which verifies the successful construction of the CN/C/BC ternary composite .

Fig. 1(c) displays the FT-IR spectra of pure BiOCl, pure $CaCO_3$ and C/BC composite. Fig. 1(d) presents the FT-IR spectra of CN/C/B compositesC, pure CN, and C/BC with various CN mass ratios. Fig. 1(c) shows that the characteristic peak at position 527cm^{-1} corresponds to the stretching vibration of Bi-O bond, while the characteristic peak at position 1407cm^{-1} is assigned to the stretching vibration of Bi-Cl bond [35,36]. The peak near position 1751, 854, and 712cm^{-1} the intense peak at position 1448cm^{-1} both originate from C-O stretching vibrations [37,38]. These results further verify the successful fabrication of the C/BC composite. On this basis, component CN was introduced into the system. As illustrated in Fig. 1(d), the absorption peaks at positions 1234 and 1643cm^{-1} are attributed to the stretching vibrations of C-N and C=N bonds, respectively, and the peak at position 808cm^{-1} matches the vibration signal of the 1,3,5-triazine isomer derived from g-C_3N_4 [32,39]. As the mass ratio of CN rises, the peak intensities corresponding to CN gradually increase, which is consistent with the XRD analysis results.

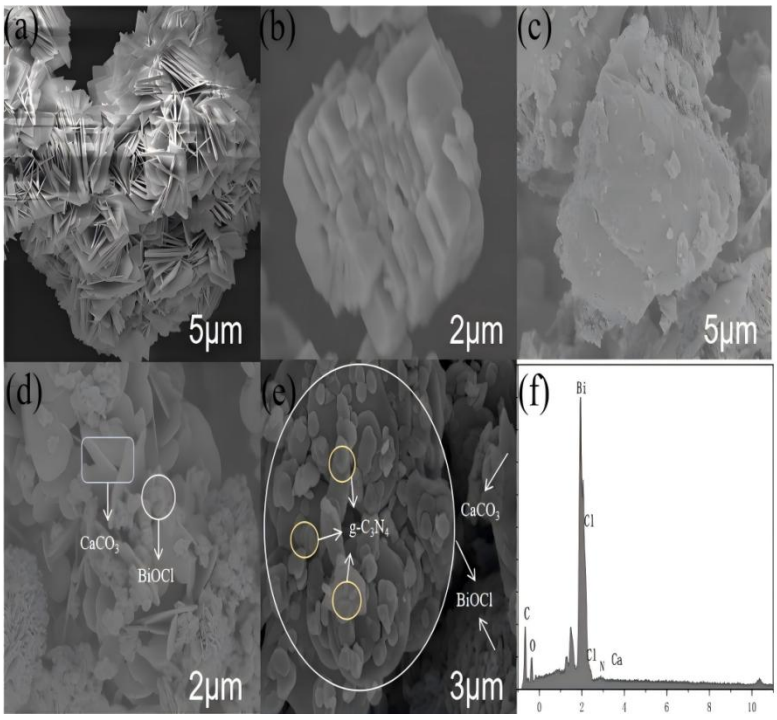


Fig. 2 (a-e) SEM images of BiOCl ,$CaCO_3$,CN ,C/BC, and X-CN/C/BC composite materials; (f) elemental mapping of CN/C/BC

Fig. 2 reveals the microstructural characteristics of the as-prepared samples. Fig. 2(a) is the SEM image of pure BiOCl, which presents spherical aggregates assembled by compact nanoparticles. The $CaCO_3$ sample in Fig. 2(b) displays calcite-like microstructures . Fig. 2(c) reveals that CN consists of

densely stacked layered nanosheets . After BiOCl was composited with $CaCO_3$, obvious structural variations can be observed from the SEM image of the binary composite in Fig. 2(d). It can be seen that BiOCl nanospheres are uniformly anchored on the surface of $CaCO_3$, which enlarges the specific surface area and provides more active sites. After introducing CN into the system Fig. 2(e) BiOCl nanospheres are homogeneously dispersed on calcite-like $CaCO_3$ substrates, and abundant sheet-like CN is grown on the exterior of BiOCl nanospheres. This structure suppresses the recombination of photogenerated electrons and holes, thereby boosting the photocatalytic activity. Fig. 2(f) presents the EDS spectrum of CN/C/BC composite, which verifies the coexistence of Bi, O, Cl, Ca, C and N elements within the sample. Further demonstrating the successful fabrication of CN/C/BC ternary composite.

3.2 Photocatalytic activity of the samples in RhB degradation

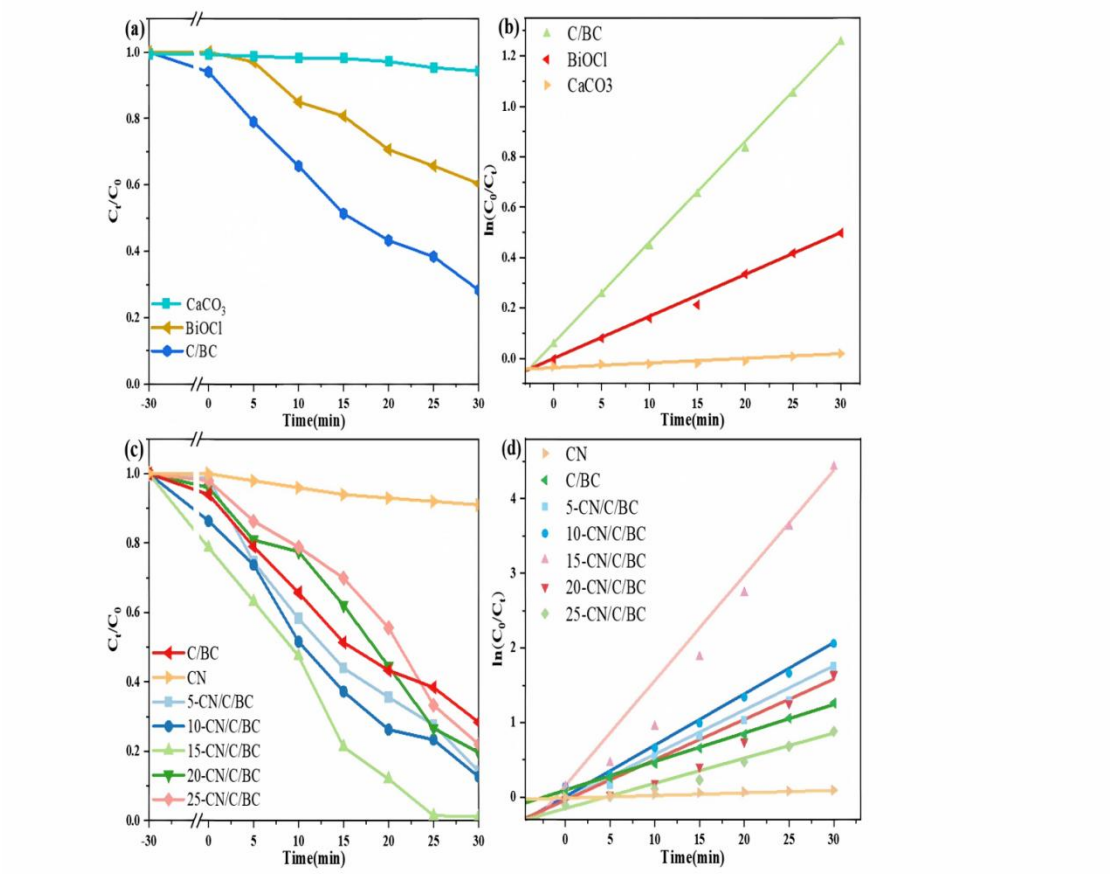


Fig. 3 (a) BiOCl, $CaCO_3$, C/BC photocatalytic degradation efficiency of RhB over time; (b) pseudo-first-order kinetic fitting curves for the degradation of RhB; (c) CN, C/BC, X-CN/C/BC photocatalytic degradation efficiency of RhB over time; (d) pseudo-first-order kinetic fitting curves for the degradation of RhB

Fig. 3(a) presents the photodegradation rate curves of RhB over BiOCl, $CaCO_3$, and C/BC. Pure BiOCl and $CaCO_3$ show negligible degradation toward RhB, achieving only 39.61% and 5% degradation efficiency within 60 min, respectively. By contrast, the C/BC composite photocatalyst attains a degradation efficiency of 71.68%, which is 1.8-fold and 14.3-fold higher than those of pure BiOCl and $CaCO_3$.

Fig. 3(b) displays the first-order kinetic curves for RhB degradation over BiOCl, $CaCO_3$, and C/BC. The kinetic equation is shown in Eq. (1-1):

$$\ln(C_0/C_t) = kt \qquad (1\text{-}1)$$

Where C_0 is the initial RhB concentration before light irradiation, C_t represents the RhB concentration after irradiation for time t (min), k denotes the reaction rate constant, and t stands for the photocatalytic reaction time (min). All samples achieved adsorption-desorption equilibrium under dark conditions within 30 min, so the adsorption contribution to the degradation process can be neglected. The RhB degradation kinetics over BiOCl, $CaCO_3$, and C/BC composites under solar-light irradiation fit well with the quasi-first-order kinetic model. As can be seen from the plot, the apparent rate constants for RhB degradation of BiOCl, $CaCO_3$, and C/BC photocatalysts are 0.01, 0.0017, and 0.042 respectively. The C/BC composite photocatalyst exhibits superior degradation performance compared with bare BiOCl and $CaCO_3$.

Photocatalytic degradation of RhB over the CN/C/BC composite under simulated sunlight. Fig. 3(c) presents the photodegradation rate curves of RhB over CN, C/BC, and X-CN/C/BC. As shown in the figure, the photocatalytic degradation efficiency of the C/BC composite towards RhB first increased and then decreased with increasing mass fraction of CN. The highest efficiency of 98.81% was achieved at a CN mass fraction of 15%, indicating that an appropriate amount of CN can effectively enhance the photocatalytic activity of the C/BC composite, while excessive loading leads to diminished performance. Fig. 3(d) the RhB degradation kinetics over BiOCl, $CaCO_3$, and C/BC composites under solar-light irradiation fit well with the quasi-first-order kinetic model. Fig. 3(d) shows the kinetic curves of RhB degradation kinetics over CN, C/BC, and X-CN/C/BC composite under solar-light irradiation fit well with the quasi-first-order kinetic model. As can be seen from the plot, the apparent rate constants for RhB degradation of C/BC, CN, and X-CN/C/BC photocatalysts are 0.042, 0.001, 0.058, 0.068, 0.147, 0.048, and 0.047 respectively, the 15-CN/C/BC composite achieves the optimal photocatalytic performance. Notably, the photocatalytic activity exhibited a volcano-shaped dependence on the CN content, first increasing and then decreasing with further addition of CN. This may be due to excessive CN cover the active sites on BiOCl surface and the light-shielding effect caused reduces light utilization, resulting in decreased photocatalytic degradation efficiency.

3.3 Photocatalytic performance cycling test

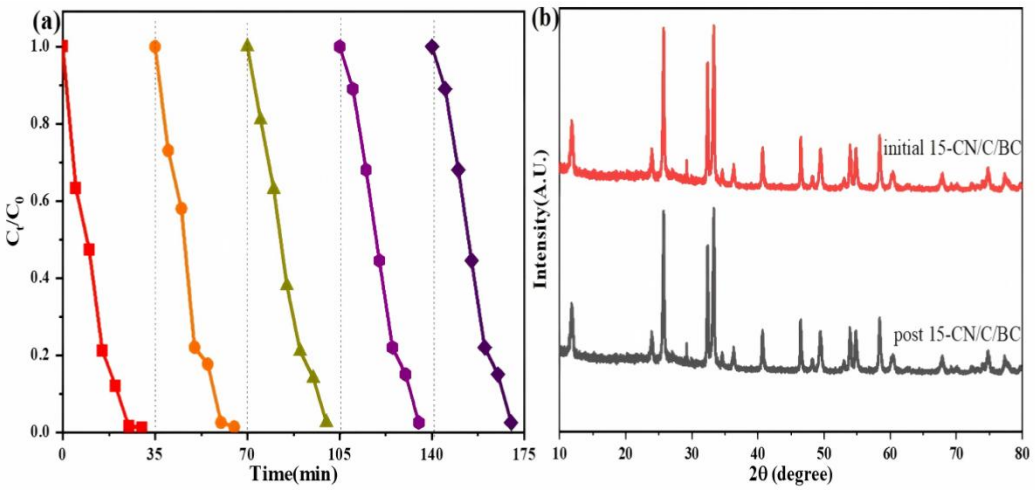


Fig. 4 (a) The com parison of 15-CN/C/BC degradation curve during the five repeated experiments; (b) XRD surveys of the used and fresh 15-CN/C/BC catalysts

To explore the stability and recyclability of the composite photocatalyst, five successive cycling tests were carried out under identical experimental conditions. As displayed in Fig. 4(a), the RhB degradation efficiency of the 15-CN/C/BC composite remained higher than 95% after each cycle, despite a slight decline relative to the first run. This minor drop can be attributed to the slight mass loss of catalyst during recovery and reuse.

Fig. 4(b) presents the comparative XRD patterns of the 15-CN/C/BC sample before and after cycling tests. No obvious variation can be detected in the crystal structure of 15-CN/C/BC before and after cyclic reactions, which confirms that the 15-CN/C/BC composite photocatalyst possesses outstanding cycling stability.

3.4 Photocatalytic enhancement mechanism

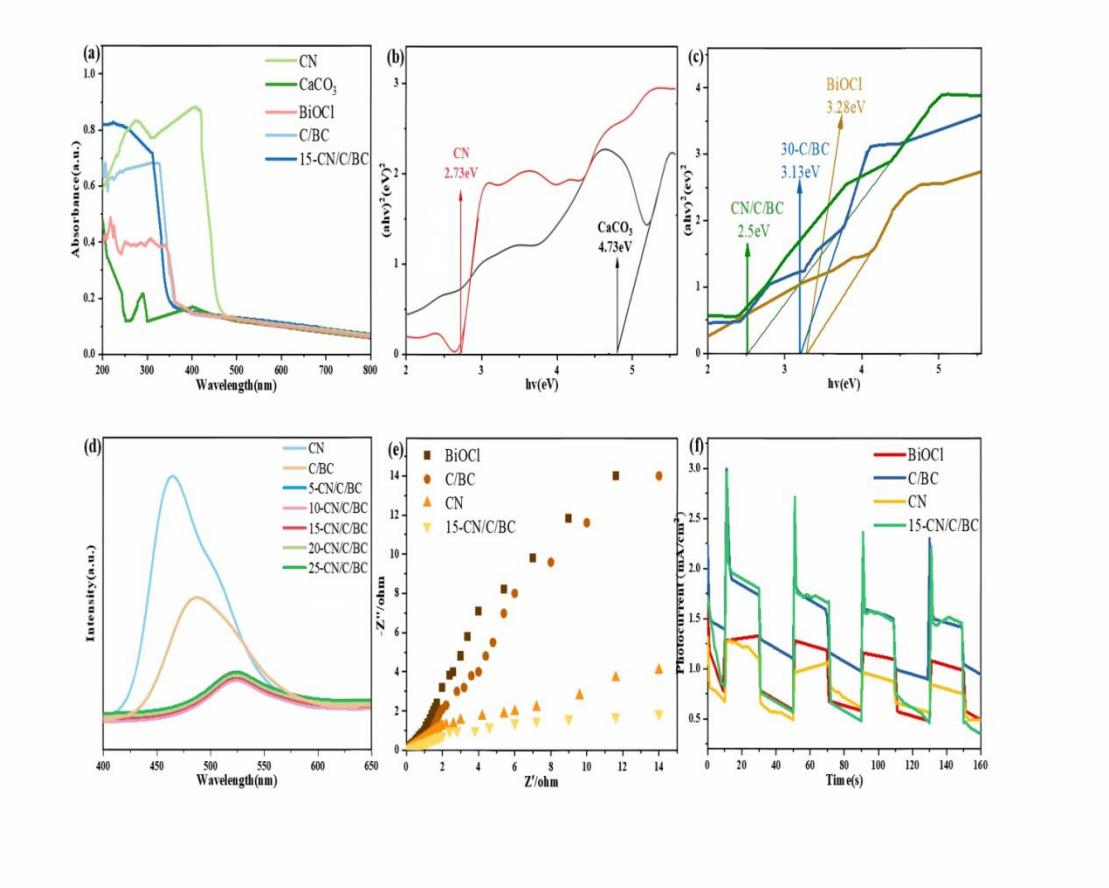


Fig. 5 (a) UV-Vis DRS spectra of BiOCl, $CaCO_3$, CN, C/BC, and 15-CN/C/BC composites; (b) Tauc plots for band gap energy of $CaCO_3$ and CN calculations; (c) Tauc plots for band gap energy of BiOCl, C/BC, and 15-CN/C/BC calculations; (d) PL spectra of CN, C/BC, and 15-CN/C/BC composite materials; (e) EIS plots of BiOCl, C/BC, CN, and 15-CN/C/BC; (f) TPC response under visible light

Fig. 5(a) shows the light absorption characteristics (UV Vis DRS) of BiOCl, $CaCO_3$, CN, C/BC, and 15-CN/C/BC composite materials. The band gap diagrams of BiOCl, $CaCO_3$, CN, C/BC, and 15-CN/C/BC composite materials are shown in Fig. 5(b, c). The band gap energy of the photocatalyst is estimated using Tauc formula (1-2):

$$\alpha h\nu = A(h\nu - Eg)^{n/2} \quad (1\text{-}2)$$

Where α is the absorption coefficient, h is Planck's constant, ν is the optical frequency, and A is a constant. The n value is determined by the type of semiconductor leap, and since both BiOCl and CN are indirect semiconductors, n is taken as 4. Fig. 5(b,c) shows the band gap of BiOCl are 3.28 eV, $CaCO_3$ are 4.73 eV and g-C_3N_4 are 2.73 eV. After adding $CaCO_3$, the absorption edge shifted and the bandgap value decreased to 3.13 eV.After adding CN to C/BC, the absorption edge of the composite material underwent a significant red shift and the bandgap value decreased to 2.5 eV. The main reason may be the narrowing of the bandgap, which produces oxygen vacancies, and the introduction of CN creates an intermediate energy level in the bandgap.

Fig. 5(d) illustrates the PL spectra of CN, C/BC, and 15-CN/C/BC composites, showing broad

emission bands within the 400-650 nm range. The emission peak intensity of CN was the highest, followed by C/BC, while 15-CN/C/BC exhibited the lowest emission intensity. The separation efficiency of photogenerated electron-hole pairs was evaluated based on PL emission intensity. A stronger emission peak indicates more severe recombination of photogenerated electrons and holes. Conversely, a weaker emission peak corresponds to more efficient separation of photogenerated carriers, which contributes to enhanced photocatalytic activity. Fig. 5(e) shows the EIS data indicate that 15-CN/C/BC exhibits the minimal charge transfer resis tance, affirming its enhanced charge migration efficiency. Fig. 5(f) shows the TPC response tests further support these findings. The 15-CN/C/BC sample demonstrates the highest photocurrent density under visible light irradiation, highlighting a markedly enhanced efficiency in the separation of photogenerated electron-hole pairs compared to the other samples. In contrast, pure BiOCl, CN, and C/BC show lower photocurrent densities, indicating less efficient carrier separation.

By bandgap values obtained through UV vis DRS can be substituted into formulas (1-3) and (1-4) to obtain the conduction band (CB) and valence band (VB) of CN, $CaCO_3$, and BiOCl :

$$E_{CB}=X-E_C-E_g/2 \quad (1\text{-}3)$$

$$E_{VB}=E_{CB}+E_g \quad (1\text{-}4)$$

Among them, X is the absolute electronegativity of the compound, and E_C is the hydrogen scale free electron energy level of about 4.5 eV.According to the formula, the conduction band (E_{CB}) and valence band (E_{VB}) of BiOCl are -0.67 eV and 2.61 eV, respectively. The conduction band (E_{CB}) and valence band (E_{VB}) of $CaCO_3$ are -4.334 eV and 0.395 eV, respectively. The conduction band (E_{CB}) and valence band (E_{VB}) of CN are -1.14 eV and 1.59 eV, respectively.

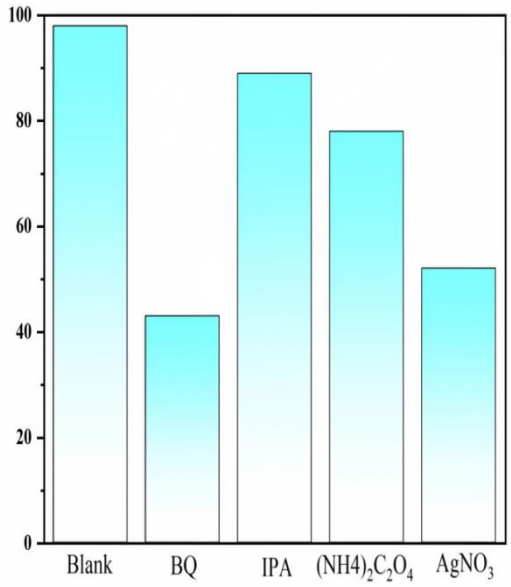


Fig. 6 Influence of different scavengers on the photocatalytic degradation efficiency of RhB

To elucidate the photocatalytic degradation mechanism, reactive species trapping experiments were performed. P-Benzoquinone (BQ), isopropyl alcohol (IPA), ammonium oxalate ($(NH_4)_2C_2O_4$), and silver nitrate ($AgNO_3$) were employed as scavengers for $\cdot O_2^-$, $\cdot OH$, h^+, and e^-, respectively. Fig. 6 shown in the figure, when BQ, $(NH_4)_2C_2O_4$, and $AgNO_3$ were separately added to the RhB solution, the photocatalytic degradation efficiency decreased markedly from 98% to 42%, 78%, and 53%, respectively.In contrast, the addition of IPA resulted in only a slight decrease in efficiency. These results indicate that $\cdot O_2^-$, h^+, and e^- are the dominant reactive species, while $\cdot OH$ plays a minor role in the degradation process. Reactive species trapping experiments demonstrated that $\cdot O_2^-$, h^+,and e^- are the primary reactive species responsible for the photodegradation of RhB over the CN/C/BC composite.

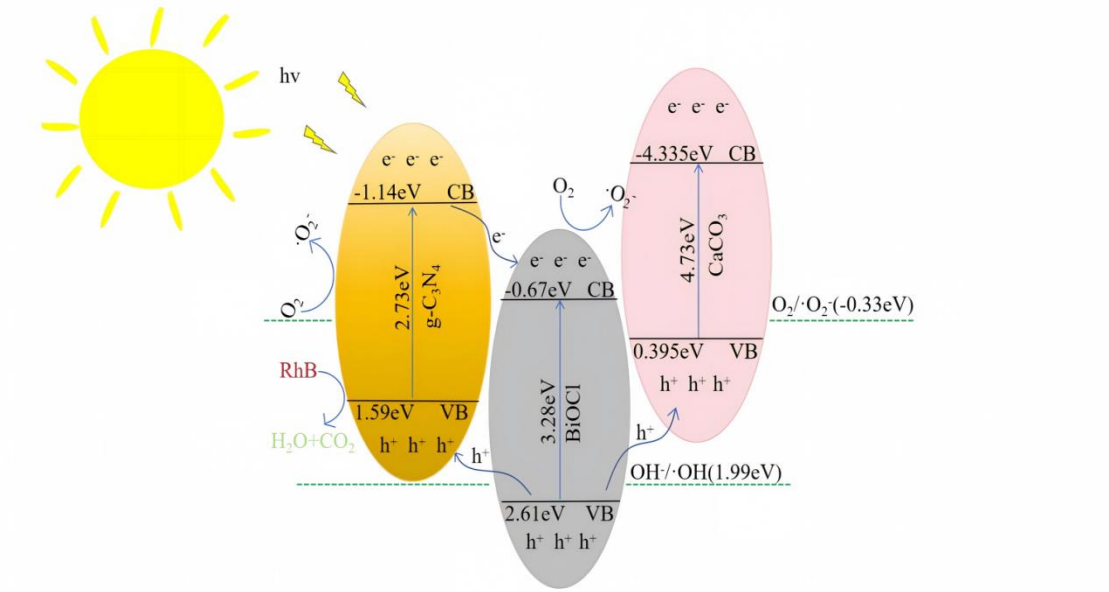


Fig. 7 Schematic illustration of the proposed photocatalytic process for RhB degradation using the 15-CN/C/BC composite material

Photocatalytic degradation mechanismBased on the band structure analysis and the results of reactive species trapping experiments, a possible photocatalytic mechanism for the degradation of RhB over the CN/C/BC composite was proposed. As illustrated in Fig. 7, under simulated solar light irradiation, BiOCl and CN are photoexcited to generate photogenerated electron-hole pairs, whereas insulating $CaCO_3$ cannot be excited. Since the valence band (VB) edge of BiOCl is more positive than those of $CaCO_3$ and CN, photogenerated holes (h^+) migrate from BiOCl to $CaCO_3$ and CN. Meanwhile, the conduction band (CB) edge of CN possesses a more negative potential than that of BiOCl, so photogenerated electrons (e^-) transfer from CN to BiOCl. This efficient charge migration achieves effective separation of massive photogenerated electrons and holes. The adsorbed RhB is oxidized to H_2O and CO_2. The valence band (VB) edge of CN is located at 1.59 eV, which is less positive than the standard redox potential of $OH^-/\cdot OH$ (+1.99 eV) [40]. Therefore, photogenerated h^+ cannot oxidize

adsorbed H_2O to produce ·OH radicals. The conduction band (CB) edge of BiOCl exhibits a more negative potential relative to the redox potential of $O_2/\cdot O_2^-$(-0.33 eV) [41]. And react with RhB to degrade it. Accordingly, the electrons accumulated on the CB of BiOCl reduce dissolved O_2 to form superoxide radicals $\cdot O_2^-$, which is in good agreement with the results of radical trapping experiments.In summary, the outstanding photocatalytic activity of the CN/C/BC composite can be attributed to the synergistic integration of its three components: the calcite $CaCO_3$ substrate provides a high-surface-area support and enhances pollutant adsorption, the combination of tetragonal-phase BiOCl and semiconductor g-C_3N_4 reduce bandgap width and effectively separate photo generated electron-hole pairs. This combination of enhanced adsorption and efficient charge separation collectively boosts the photocatalytic degradation efficiency.

4. Conclusion

In this work, $CaCO_3$/BiOCl composite was first fabricated by a solvothermal route. Afterwards, the pre-synthesized g-C_3N_4 was hybridized with $CaCO_3$/BiOCl via physical stirring to construct ternary g-C_3N_4/$CaCO_3$/BiOCl composite photocatalyst. Furthermore, its photocatalytic degradation performance was systematically evaluated. The 15-g-C_3N_4/$CaCO_3$/BiOCl composite photocatalyst delivers outstanding photocatalytic activity, achieving a maximum RhB degradation efficiency of 98.81%.The enhanced catalytic performance can be explained as follows: calcite-phase $CaCO_3$ enlarges the specific surface area of BiOCl and supplies abundant surface active sites, meanwhile, composite of BiOCl and g-C_3N_4, which narrows the band gap of the composite. This structure suppresses the recombination of photogenerated electron-hole pairs and ultimately boosts the overall photocatalytic efficiency. The introduced $CaCO_3$ and g-C_3N_4 possess the advantages of facile preparation, low cost, non-toxicity and environmental friendliness. This work provides a new insight into the design and fabrication of high-efficiency photocatalysts for wastewater purification. Future studies can focus on developing more low-cost, efficient and eco-friendly composite photocatalysts to further enhance structural stability and expand practical application prospects.

References

[1] Kang S, Liu W, Wang Y (2022) Starch-derived flocculantwith hyperbranched brush architecture for effectively flocculating organic dyes,heavy metals and antibiotics.Journal of the Taiwan Institute of Chemical Engineers 135:104383

[2] Yuan Y, Zhang J, Xing L (2019) Effective electrochemicaldecolorization of azo dye on titanium suboxide cathodein bioelectrochemical system. International Journal of Environmental Science and Technology 16:8363-8374

[3] Xia JX, Wang B, Di J (2022) Construction of singleatom catalysts for electrophoto and photoelectron catalytic applications: State of-the-art,opportunities and challenges.Materials Today 53 :217-237

[4] Liu FX, Sun B, Liu ZY, Wei YQ, Gao TT, Zhou GW (2024) Vacancy engineering mediated hollow structured ZnO/ZnS S-scheme heterojunction for highly efficient photocatalytic H_2 production. Catalysts 64: 152-165

[5] Liu T, Wang B, Wang T (2022) One-pot synthesis of Zn-CdS@C nanoarchitecture with improved photocatalytic performance toward antibiotic degradation. Chemosphere 300:134621

[6] Yuan F, Sun ZM, Li CQ, Tan Y (2020) Multi-component design and in-situ synthesis of visible-light-driven SnO_2/g-C_3N_4/diatomite composite for high-efficient photoreduction of Cr (VI) with the aid of citric acid.Journal of hazardous materials 396:122694

[7] Liu JW, Shi J, Deng HP (2023) Current status of research on BiOX-based heterojunction photocatalytic systems: Synthesis methods, photocatalytic applications and prospects.Journal of Environmental Chemical Engineering 5:11

[8] Maitlo HA, Anand B, Kim KH (2024) TiO_2-based photocatalytic generation of hydrogen from water and wastewater. applied energy 361:122932

[9] Zhang RX, Shi JL, Fu L (2024) Direct photocatalytic methane oxidation to formaldehyde by N doping co-decorated mixed crystal TiO_2. ACS Nano 18:12994-13005

[10] Yang M, Yang Q, Zhong JB (2017) PVA-assistedhydrothermal preparation of BiOF with remarkably enhanced photocatalytic performance. Materials Letters 201:35-38

[11] Song SJ, Xing ZP, Wang K (2023) 3D f lower-likemesoporous $Bi_4O_5I_2$/MoS_2Z-scheme heterojunction withoptimized photothermal-photocatalytic performance.Green Energy & Environment 8:200-212

[12] Zhao GQ, Hu J, Zou J (2022) Modulation of BiOBr-basedphotocatalysts for energy and environmental application: A critical review. Journal of Environmental Chemical Engineering 10:107226

[13] Li WJ, Wang X, Zhang YP (2022) BiOX/Bi/BiOX(X=Cl,Br)double-side nanosheet arrays:synthesis,structures,and photo(electro) catalytic applications. Advanced Materials Interfaces 19:2200260

[14] Hussain A, Hou JH, Tahir M (2022) Recent advances in BiOX-based photocatalysts to enhanced efficiency for energy and environment applications. Catalysis Reviews 29:1-55

[15] Zheng J, Liu J, Feng X (2023) Outstanding photo-thermo synergy inaerobic oxidation of cyclohexane by bismuth tungstate-bismuthoxychloride high-low heterojunction.Journal of Colloid and Interface Science 651:304-318

[16] Wei S, Zhong H, Wang H (2022) Oxygen vacancy enhanced visiblelight photocatalytic selective oxidation of benzylamine over ultrathin Pd/BiOCl nanosheets. Applied Catalysis B: Environmental 305:121032

[17] Yao D, Liang K, Chen G (2023) Dual-functional reaction strategyboosts carbon dioxide reduction by coupling with selective benzylalcohol oxidation on nano-Au/BiOCl photocatalysts. Journal of Catalysis 422:56-68

[18] Anirban D, Inna H, Hani G (2018) Solar photocatalytic degradation of trace organic pollutants in water by Bi(0)-doped bismuth oxyhalide thin films. ACS Omega 3:10858-10865

[19] Yuan Q, Wei S, Hu T (2021) Defect-modified ultrathin BiOX(X=Cl,Br) nanosheets via a top-down approach witheffective visible-light photocatalytic degradation.Journal of physical chemistry 34:18630-18639
[20] Liu WW, Zhong DL, Dai ZQ (2019) Synergetic utilization of photoabsorption and surface facet in crystalline/amorphous contacted BiOCl-Bi_2S_3 composite for photocatalytic degradation. Journal of Alloys Compounds 780:907-916
[21] Wang Ml, Han YM, Peng HQ (2024) Boosting the electrocatalytic activity of 2D ultrathin BiOX/rGO (X = F, Cl, Br, and I) nanosheets as sulfur hosts. Inorgnic Chemistry Frontiers 11 4277-4287
[22] Tian YH, Li Sl, Zhang GX (2024) Enhanced photocatalytic performance of BiOBr/Kao linite composite. Chemistryselect 7:4187
[23] Liu ZS, Bi YH, Zhao YL (2014) Synthesis and photocatalytic property of BiOBr/palygorskite composites. Materials Research Bulletin 49:167-171
[24] Zhang G, Sun Z, Hu X (2017) Synthesis of BiOCl/TiO_2–zeolite composite with enhanced visible light photoactivity. Journal of the Taiwan Institute of Chemical Engineers 81:435-444
[25] Gao X, Chen YQ, Kang ZW (2021) Enhanced degradation of aqueous tetracycline hydrochloride by integrating eggshell-derived $CaCO_3$/CuS nanocomposite with advanced oxidation process. Molecular Catalysis 501:111380
[26] Cui W, Li JY, Chen LC (2020) Nature-inspired $CaCO_3$ loading TiO_2 composites for efficient and durable photocatalytic mineralization of gaseous toluene. Science Bulletin19:1626-1634
[27] Wang J, Sun SJ, Pan L (2010) Preparation and properties of $CaCO_3$-supported nano-TiO_2 composite with improved photocatalytic performance. Materials 12:3369
[28] Hu YY, Hu XY, Xue L (2022) Preparation of $CaCO_3$ mediated BiOBr that rich (110) facet andresearch of the photocatalytic properties. Applied Surface Science 598:153800
[29] Muhammad AK, Sadaf M, Imrana SH (2025) Recent advances over the doped g-C_3N_4 in photocatalysis: A review. Coordination Chemistry Reviews 1:216227
[30] Kalidasan K, Mallapur S, MunirathnamK (2024) Transition metals-doped g-C_3N_4 nanostructures as advanced photocatalysts for energy and environmental applications. Chemosphere 352:141354
[31] Xu TR, Wang GH, Liu ZH (2024) Construction of magnetically separable S-scheme $BiFeO_3$/Cl-g-C_3N_4 heterostructure photocatalyst for simultaneous removal of Cr(VI) and tetracycline in aqueous solution: Performance and mechanism insight[J]. Journal of Catalysis 440: 115821
[32] Yang CY, Rong QY, Shi FY (2024) Rationally designed S-scheme heterojunction of BiOCl/g-C_3N_4 for photodegradation of sulfamerazine. Chinese Chemical Letters 35:109767
[33] Bai X, Wang Y, Zang RB (2021) Preparation and Visible-Light Photocatalytic performance of BiOCl/In_2S_3 Composite. Chemical Bulletin 11:1224-1230
[34] Zheng T, Yi H, Zhang S (2020) Preparation and formation mechanism of calcium carbonatehollow microspheres. Journal of Crystal Growth 549:125870
[35] Tao T, Dai, Yang JR (2015) Synthesis, characterization and photocatalytic properties of BiOBr/amidoxime fiber composites. Materials Science in Semiconductor Processing 40:344-350
[36] Zhu Z, Zhao X, Xiao X (2022) Mechanistic insights into the formation of surface oxygenvacancies with controllable concentration and long-term stability in small-molecule bondedbismuth-based semiconductor hybrid photocatalyst.Journal of colloid and interface science 625:109-18

[37] Ramasamy V, Anand P, Suresh G (2018) Synthesis and characterization of polymer-mediated $CaCO_3$ nanoparticles using limestone: a novel approach.Advanced Powder Technology 29:818-834
[38] Tovani CB, Oliveira TM, Gloter A (2018) Sr^{2+}-substituted $CaCO_3$ nanorods: impact on the structure and bioactivity.Crystal Growth and Design 18:2932-2940
[39] Ran J, Guo W, Wang H (2018) Metal-free 2D/2D phosphorene/g-C_3N_4 van der waals heterojunction for highly enhanced visible-light photocatalytic H_2 production.Advanced Materials 30: 2-7
[40] Fu JSM, Zhang XT (2006) Titanium dioxide photocataly-sis: Present situation and futureapproaches. Comptes Rendus Chimie 6:750-760
[41] Chen C C, Ma WH, Zhao JC (2010) Semiconductor-mediated photodegradation of pollutans under visible-light irradi-ation. Chemical Society Reviews 11:4206-4219

Supplementary Files

This is a list of supplementary files associated with this preprint. Click to download.

- Graphicalabstract.jpeg